

<https://doi.org/10.1038/s41612-024-00717-y>

The role of Arctic sea ice loss in the interdecadal trends of the East Asian summer monsoon in a warming climate

Check for updates

Xiaoqi Zhang^{1,2}, Bian He²✉, Qing Bao²✉, Yimin Liu^{2,3}, Guoxiong Wu^{2,3}, Anmin Duan⁴,
Wenting Hu², Chen Sheng² & Jian Rao¹

The East Asian summer monsoon precipitation has exhibited a well-known “southern China flood and northern China drought” pattern in recent decades. The increase in aerosols and warming oceans are recognized as two important forcings that control of the precipitation trends over East Asian land. However, in this study, by using large ensemble simulations from the CMIP6 Polar Amplification Model Intercomparison Project (PAMIP), the influence of Arctic amplification, serving as the prominent feature of global warming, is very important in modulating the East Asian summer precipitation pattern, which is comparable to the influence of sea surface temperature (SST). Additionally, the observed “southern China flood and northern China drought” pattern only exists in July and August, whereas a triple pattern with the precipitation positive anomaly center over Middle China occurs in June. These patterns are closely connected with the regional differences in Arctic sea ice loss from June to July, affected through both the Rossby waves propagating in a weaker westerly jet and the decrease in the large-scale meridional thermal contrast in a warming climate.

The East Asian summer monsoon (EASM) system is an important component of the global monsoon system, which is modulated by multiple complex forcings with a wide range of time scales^{1–14}. With the rapid increase in greenhouse gases (GHGs) since the middle of the 20th century, EASM precipitation exhibits a well-known “southern China flood and northern China drought” pattern and is associated with surface air temperature cooling for the June–July–August interdecadal trends. Numerous studies have revealed that the increase in anthropogenic aerosols, such as black carbon and sulfate, is the dominant control factor over surface cooling and increasing precipitation over South China^{15–23}, while other studies have emphasized that warming oceans in the tropics provide more water vapor fluxes and lead to an increase in East Asian summer precipitation^{24–27}. However, except for the contributions of the local anthropogenic aerosol forcing over East Asia land and the sea surface temperature (SST) forcing at low latitudes, the contributions of Arctic sea ice, which undergoes a rapid decrease under global warming, to this trend have received less attention.

The climate impact of Arctic sea ice loss and Arctic amplification have been extensively studied in recent decades^{28–39}, but most studies mainly

focus on boreal winter seasons, and the conclusions are still controversial due to the inconsistency between the observational analysis and numerical modeling. Observational studies highlight that Arctic sea ice loss is closely connected to changes in the north hemispheric mid-latitude circulation and associated weather and climate system during boreal winter, such as surface cooling over the Eurasian continent, intensification of the Siberian High, weakening of the westerly jet, increasing snowfall and increasing extreme cold events^{35,40–43}. However, the model responses to the Arctic sea ice forcing are diverse, and the model signals are quite weak and not easily discerned from noise^{32,43–49}. A large ensemble simulation has been proposed to reduce the noise in climate simulations in recent years, and more robust responses can be derived based on such experiments and additional statistical constraints^{50–52}. In the Polar Amplification Model Intercomparison Project (PAMIP) of the Sixth Coupled Model Intercomparison Project (CMIP6)⁵³, the responses of atmospheric circulation to the changes in Arctic sea ice and SST will be examined by a set of coordinated large ensemble simulations with prescribed SST and sea ice concentration (SIC) for present-day (pd), pre-industrial (pi), and future (fut) scenarios⁵⁴. Based on the above datasets,

¹Key Laboratory of Meteorological Disaster, Ministry of Education (KLME) / Joint International Research Laboratory of Climate and Environment Change (ILCEC) / Collaborative Innovation Center on Forecast and Evaluation of Meteorological Disasters (CIC-FEMD), Nanjing University of Information Science and Technology, Nanjing, 210044, China. ²State Key Laboratory of Numerical Modeling for Atmospheric Sciences and Geophysical Fluid Dynamics (LASG), Institute of Atmospheric Physics, Chinese Academy of Sciences, Beijing, 100029, China. ³College of Earth and Planetary Sciences, University of Chinese Academy of Sciences, Beijing, 100049, China. ⁴State Key Laboratory of Marine Environmental Science, College of Ocean and Earth Sciences, Xiamen University, Xiamen, 361005, China.

✉ e-mail: heb@lasg.iap.ac.cn; qbao@lasg.iap.ac.cn

a recent study showed that state-of-the-art models could capture the surface cooling over eastern Eurasian land and the weakening of mid-latitude westerlies in response to projected Arctic sea ice loss by analyzing 3000 samples of simulations⁵⁵. This study also implies that the robust response of the Eurasian summer climate to Arctic sea ice loss can be investigated in such a manner.

Compared to the tremendous and systematic analysis of the climate effects of Arctic sea ice loss during winter seasons, studies of the influences of Arctic sea ice loss on East Asian summer monsoon precipitation are relatively rare, and the understanding of these influences is still not clear. Previous studies have mainly focused on the interannual influence of spring Arctic sea ice loss on summer rainfall in China. Numerous studies have proposed that Arctic sea ice loss could result in a dipole precipitation anomaly pattern over East Asian land, with a positive center in central China and a negative center in southern China^{20,56,57}. However, other studies show that the decrease in Arctic sea ice will result in the weakening of the EASM and produce more summer precipitation over South China⁵⁸. Moreover, the contribution of Arctic sea ice loss to the decadal trends of East Asian summer precipitation has seldom been discussed. Thus, in this study, based on large samples of multimodel simulations under pd and pi forcings in PAMIP and by using observation constraints, the role of Arctic sea ice loss on the EASM decadal trends is revealed, and the relative contributions between SIC and SST and the associated physical mechanism are also discussed. This study provides an understanding of the formation of interdecadal trends in the EASM under global warming.

Results

The observed EASM interdecadal trends from 1951 to 2000

The observed interdecadal trends of EASM precipitation and 850 hPa wind from 1951 to 2000 are investigated in this study. There are three reasons for adopting this period. First, the global surface temperature increased rapidly after the 1950s, driven by well-mixed greenhouse gases (GHGs) related to human activities, while global precipitation over land has likely increased since 1950 and increased rapidly after the 1980s⁵⁹. The global warming hiatus appeared after the 2000s, which implies that natural variability makes an important contribution to the continuous global warming trend^{60–62}. The interdecadal variability in precipitation also shows considerable variation after the 2000s. For example, we present the time series of precipitation over East Asian land during June–July–August from 1901 to 2019 in Supplementary Fig. 1 based on GPCP datasets. A 10-year running mean is applied to filter the interannual variabilities. It is clear that there are significant changes in precipitation during this period, while the application of satellite observations after 1979 makes precipitation data more reliable. Thus, the use of the period of 1951 to 2000 will be a better choice for understanding the EASM interdecadal trend responses to imposed external forcings. Second, according to the design of the PAMIP, the 1979–2008 global mean surface temperature is defined as the present-day forcing, while the removal of the estimate of the global warming index (0.57 °C) is used to derive the pre-industrial forcing. The magnitude of the SST forcing between present-day and pre-industrial times is comparable to the interdecadal trends from 1951 to 2000. Finally, this period is frequently studied in previous literature^{15,17,21,26,27}. Thus, the analysis in this study can also be compared with previous related works to some extent. It is worth noting that the current study does not include recent decades.

The observed interdecadal trends of EASM precipitation and 850 hPa winds are investigated for June, July, and August. It is quite surprising that the traditional “southern China flood and northern China drought” pattern only appears in July (Fig. 1b) and August (Supplementary Fig. 2), with a meridional dipole precipitation pattern and northeast wind anomaly over East Asia. However, in June, the precipitation trend shows a triple pattern with an increased center in middle China and two decreased centers in northern and southern China. The 850 hPa wind trend shows a regional cyclonic circulation, which favors the precipitation increase in central China. In summary, the precipitation trend pattern in June is roughly reversed in July and August, which implies that the causes and associated

physical processes of the precipitation trends from June to July greatly differ. Since the precipitation patterns in July and August are quite similar, we only compare the analysis between June and July in the following sections.

EASM responses to SST and SIC forcings in a warming climate

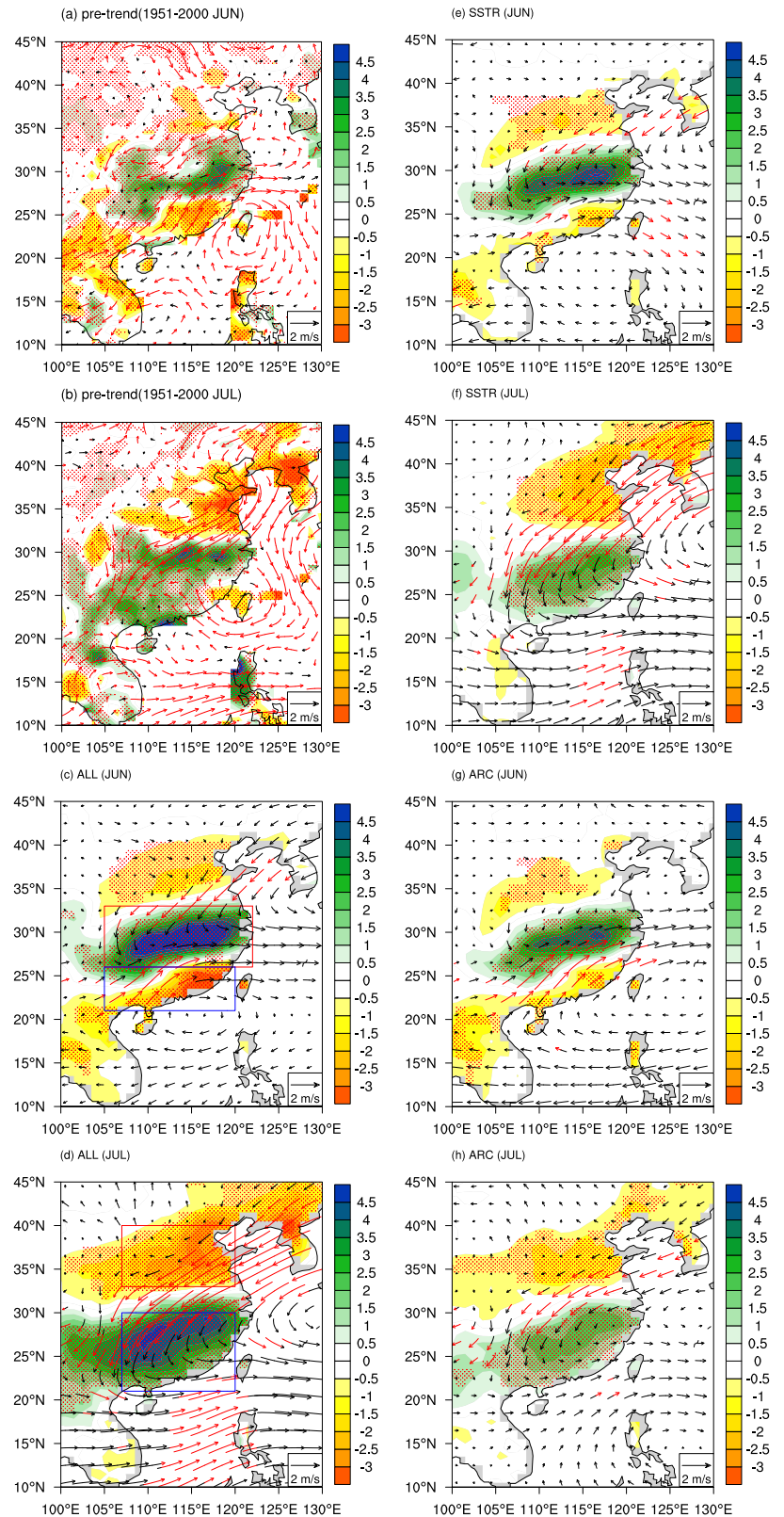
The EASM precipitation and 850 hPa wind responses to the difference between present-day and pre-industrial forcings from PAMIP experiments (Table 1) are recognized as the responses of the monsoon system to overall global warming and are first examined. To reduce the influences from the model bias on the model responses, an observation constraint method is applied (see Methods) to the precipitation simulation in June (Fig. 1c) and July (Fig. 1d). The experiment_id “ALL” denotes the model responses to changes in both SST and SIC. In June, the constrained precipitation anomaly shows a clear meridional triple pattern with increasing precipitation in central China and decreasing precipitation in both northern and southern China, which is very similar to the observed trends (Fig. 1a). The corresponding 850 hPa wind responses show a clear cyclonic shear over the precipitation positive anomaly center, which is also close to the observed pattern. Over the ocean regions, an anticyclone anomaly is simulated over the South China Sea, which is west of the observed anticyclone. In July (Fig. 1d), the model response in ALL reproduced the traditional “southern China flood and northern China drought” pattern. The simulated 850 hPa wind shows strong northeast air flows over East Asian land and a uniform westerly over subtropical ocean regions, which is close overall to the observed wind trends (Fig. 1b). The above analysis indicates that the constrained multimodel mean responses could capture the observed interdecadal trends of the EASM well. This result provides a robust basis for understanding the individual effects of SST increase and Arctic SIC loss on the EASM.

We show the EASM responses to the separate SST and Arctic SIC forcing in Fig. 1e–h. The SSTR (Table 1) is the model response between the present-day and pre-industrial SST forcings when keeping the SIC forcing unchanged. The simulated precipitation in June (Fig. 1e) shows a clear meridional triple pattern over East Asia, which is also very similar to the results in ALL (Fig. 1c), except that the intensity is slightly weak. The 850 hPa wind mainly shows cyclonic shear over the precipitation. Interestingly, the precipitation responses to only Arctic sea ice loss (Fig. 1g) also show a meridional triple pattern similar to that in SSTR and ALL, which indicates that the contributions from Arctic sea ice loss to EASM cannot be neglected. The 850 hPa wind mainly shows an anticyclonic anomaly over the western Pacific and is quite different from the wind response in the SSTR, which implies that the formation mechanisms of the triple patterns in the SSTR and ARC are different. In July, the precipitation responses to SST and SIC both exhibit the traditional dipole pattern, while the precipitation intensity in the ARC is overall slightly weaker than that in the SSTR. The 850 hPa wind responses in SSTR and ARC both appear as large-scale cyclonic anomalies over East Asia, which are both similar to those in ALL (Fig. 1d), except that the response in ARC is slightly weaker. These results indicate that both the SST increase and Arctic sea ice loss contribute to the interdecadal trends of the EASM. Moreover, the results highlight that the influences from Arctic sea ice loss are almost as important as the SST increase.

To quantitatively understand the role of Arctic sea ice loss on the precipitation trends over East Asia, we created a box plot to understand the distributions of precipitation responses in each experiment (Fig. 2). Figure 2a shows the precipitation response in central China in June (red box in June, Fig. 1c). The precipitation anomaly in ALL ranges from $-0.92 \text{ mm day}^{-1}$ to 7.73 mm day^{-1} , with a mean value of 2.70 mm day^{-1} . The precipitation response to SST only (SSTR) shows a larger range ($-2.55 \text{ mm day}^{-1}$ to 9.70 mm day^{-1}) than in ALL, with a mean value of 1.86 mm day^{-1} . Finally, the precipitation response to SIC only (ARC) shows the largest range from $-2.43 \text{ mm day}^{-1}$ to $11.10 \text{ mm day}^{-1}$, with a mean value of 1.72 mm day^{-1} .

Two important features can be derived from this box plot. First, the quantitative calculation showed that the influence of Arctic sea ice loss on the increasing trend over central China is as important as SST.

Fig. 1 | Trends and responses of precipitation and 850 hPa wind in June and July. Precipitation (shading, units: mm day^{-1}) and 850 hPa wind (vector, units: m s^{-1}) trends in June (a) and July (b) for GPCC/ERA5 during 1951–2000. The precipitation (shading, units: mm day^{-1}) and 850 hPa wind (vector, units: m s^{-1}) responses to ALL in June (c) and July (d). The precipitation (shading, units: mm day^{-1}) and 850 hPa wind (vector, units: m s^{-1}) responses to SSTR in June (e) and July (f). The precipitation (shading, units: mm day^{-1}) and 850 hPa wind (vector, units: m s^{-1}) responses to ARC in June (g) and July (h). The red box represents the northern part of East Asia (26°N – 33°N , 105°E – 122°E in Fig. 1c) (33°N – 40°N , 107°E – 120°E in Fig. 1d), and the blue box represents the southern part of East Asia (21°N – 26°N , 105°E – 120°E in Fig. 1c) (21°N – 30°N , 107°E – 120°E in Fig. 1d). Stippling and red vectors indicate where the trends or the multimodel ensemble mean response is significant (90% confidence).



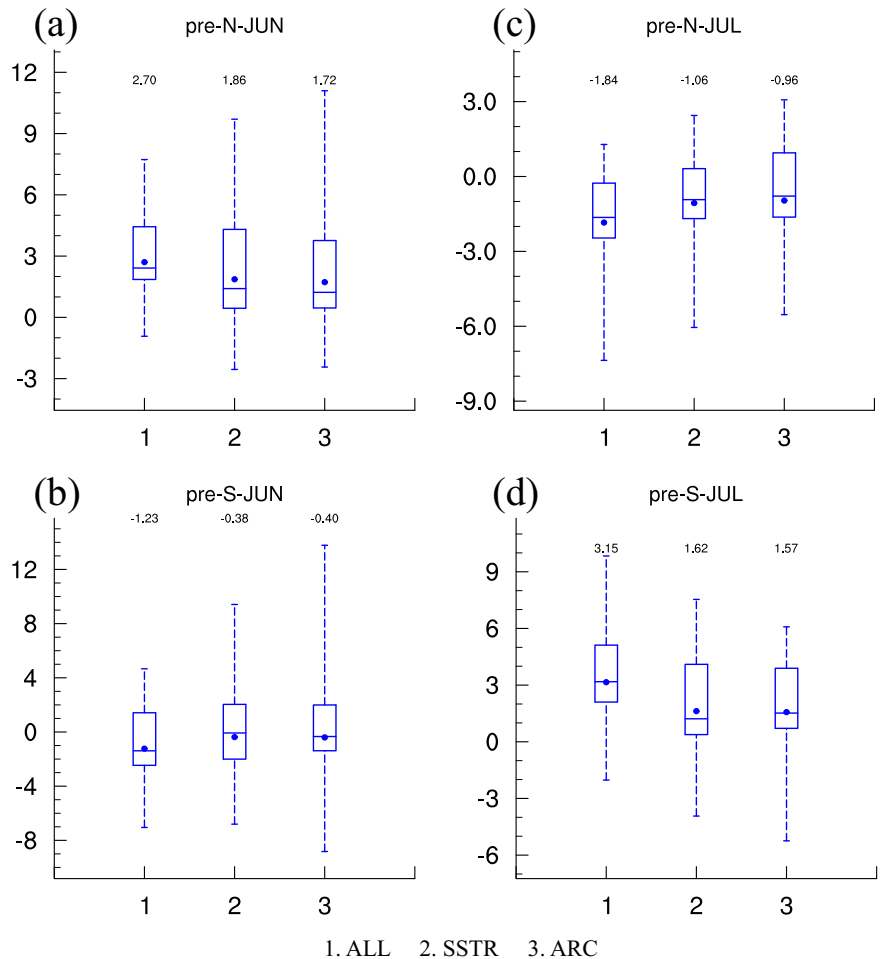
Moreover, the linear response of precipitation in the northern region in June to SSTR and ARC is 3.58 mm day^{-1} ($\text{PRE}_{\text{SSTR}} + \text{PRE}_{\text{ARC}}$), which is higher than the value of 2.70 mm day^{-1} when the two forcings are prescribed together in the model (Fig. 2a). This suggests that nonlinear interactions of SST and SIC have weakened this response. Second, the precipitation responses to Arctic sea ice loss appear to

have the largest uncertainty, which implies that the EASM response is quite sensitive to the Arctic sea ice forcing, especially in June. However, for the precipitation decrease trend over South China in June (Fig. 2b), the mean precipitation anomaly in ALL is $-1.23 \text{ mm day}^{-1}$, which is lower than the linear sum of the precipitation anomalies in SSTR ($-0.38 \text{ mm day}^{-1}$) and ARC ($-0.40 \text{ mm day}^{-1}$). This result

Table 1 | Introduction to the PAMIP experiments used in the research

Number	Experiment Name	Description
No.1	pdSST-pdSIC	Time slice forced by climatological monthly mean SST and SIC for the present day (pd).
No.2	piSST-piSIC	Time slice forced by climatological monthly mean SST and SIC for pre-industrial (pi) conditions.
No.3	piSST-pdSIC	Time slice forced by pi SST and pd SIC.
No.4	pdSST-piArcSIC	Time slice forced by pd SST and pi Arctic SIC.
No.5	ALL	pdSST-pdSIC (NO.1) minus piSST-piSIC (NO.2) to characterize the response of the atmosphere to SST rise and SIC loss.
No.6	SSTR	pdSST-pdSIC (NO.1) minus piSST-pdSIC (NO.3) to characterize the response of the atmosphere to SST rise.
No.7	ARC	pdSST-pdSIC (NO.1) minus pdSST-piArcSIC (NO.4) to characterize the response of the atmosphere to Arctic SIC loss.

Fig. 2 | Box plot analysis of precipitation in June and July. Precipitation averages over the northern (a) (26°N–33°N, 105°E–122°E, as red box in Fig. 1c) and southern (b) (21°N–26°N, 105°E–120°E, as blue box in Fig. 1c) regions in June. Precipitation averages over the northern (c) (33°N–40°N, 107°E–120°E, as red box in Fig. 1d) and southern (d) (21°N–30°N, 107°E–120°E, as blue box in Fig. 1d) regions in July. The box plot represents the maximum value, upper quartile, median, lower quartile, and minimum value, while the dots indicate the area-averaged precipitation of the ensemble mean.



indicates that the combined effect of SST and SIC amplifies the influence of individual SST and SIC on the precipitation trend over South China in June.

The quantitative calculations for the precipitation dipole pattern in July are shown in Fig. 2c, d, respectively. There are two main features that are quite different from the precipitation trends in June. First, the sums of the mean precipitation anomaly ($-2.02 \text{ mm day}^{-1}$ in the northern area and 3.19 mm day^{-1} in the southern area) in the SSTR and ARC are both very close to the means in ALL ($-1.84 \text{ mm day}^{-1}$ for the northern area and 3.15 mm day^{-1} for the southern area), which denotes that the mean combined effect of SST and SIC on EASM precipitation is quite close to the sum of the mean individual effect from the SST and SIC forcing in July. Second, the range of the precipitation response in the ARC is -5.53 to 3.07 mm day^{-1} in the northern region and -5.24 to 6.09 mm day^{-1} in the southern region,

which are close to the precipitation ranges in the ALL and SSTR. This result implies that the precipitation response to the Arctic sea ice forcing is less sensitive in July than in June. To understand the associated atmospheric circulations and hydrological cycle in response to the different forcings, we analyze the atmospheric moisture budgets in the following sections.

Moisture budgets diagnostics

The diagnostic equation of the moisture budget (Eq. 2, see Methods) has conventionally been used for understanding the hydrological cycle responses to external forcings in climate dynamics studies^{63–65}. As shown in Eq. 3, the precipitation responses to the external forcing can be calculated by the difference between perturbed evaporation and water vapor transport in the atmosphere. In this study, since the response of evaporation is quite small and can be neglected in all the experiments, we only show the responses of vertical

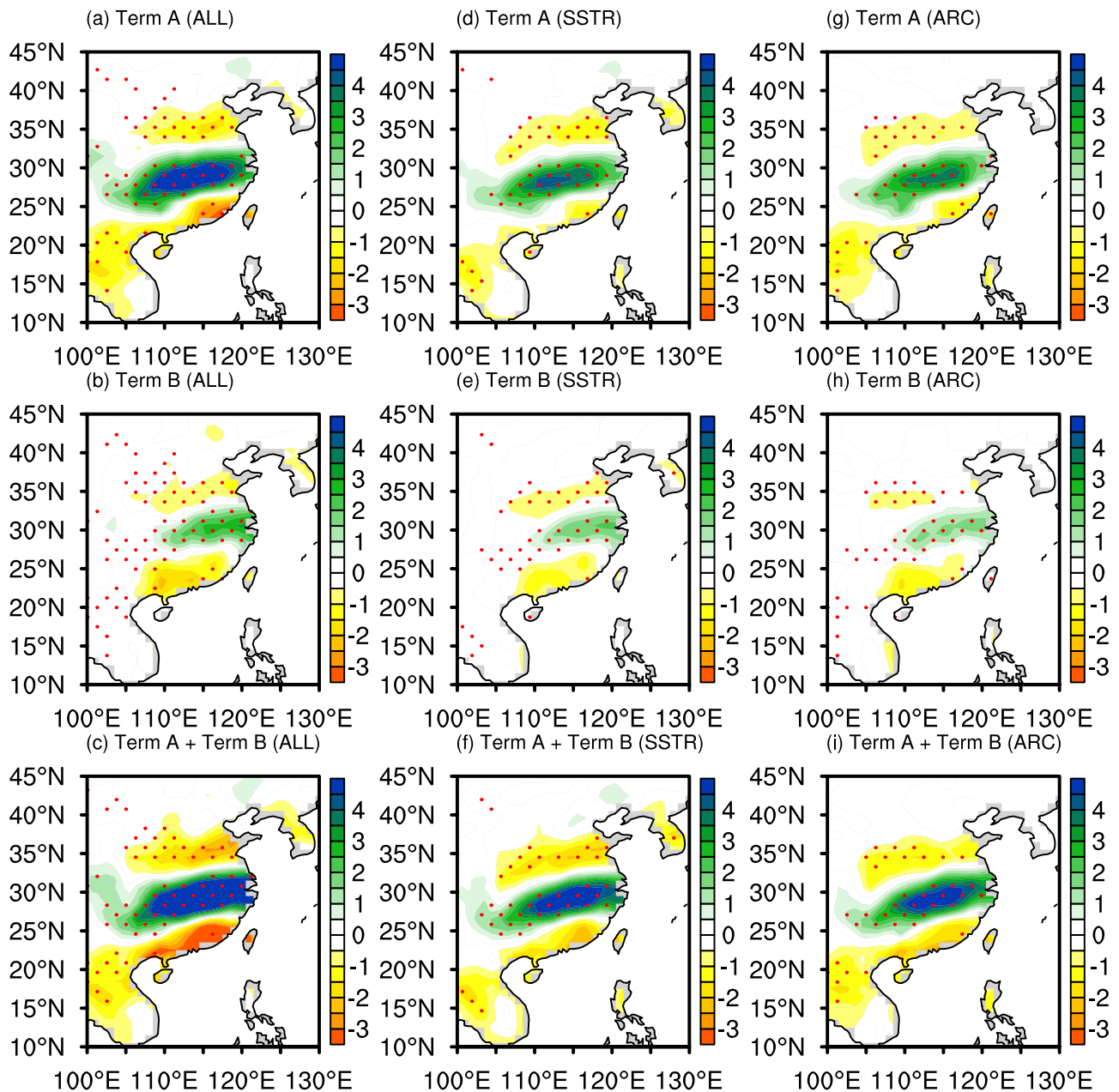


Fig. 3 | Moisture processes driving changes in the precipitation anomaly (June). The vertical transport differences in water vapor ($-\langle \omega \partial_p q' \rangle$, units: mm day^{-1}) responses to ALL (a), SSTR (d) and ARC (g). The horizontal transport differences in water vapor ($-\langle \mathbf{V}_h \cdot \nabla_h q' \rangle$, units: mm day^{-1}) responses to ALL (b), SSTR (e) and

ARC (h). The total transport differences in water vapor ($-\langle \omega \partial_p q' \rangle - \langle \mathbf{V}_h \cdot \nabla_h q' \rangle$, units: mm day^{-1}) responses to ALL (c), SSTR (f) and ARC (i). Stippling indicates where the multimodel ensemble mean response is significant (90% confidence).

and horizontal transport of water vapor for different experiments in Figs. 3 and 4, while the evaporation term together with the residual term are shown in Supplementary Material (Supplementary Figs. 3, 4).

In general, the sum of the advection terms (Fig. 3c, f, i) reproduces the meridional triple pattern of precipitation responses in June well, as shown in Fig. 1c, e, g for all the experiments, which indicates that the external transport of water vapor is crucial for the changes in precipitation under different forcings. Moreover, the vertical transport terms (Fig. 3a, d, g) appear as the dominant term for the positive precipitation anomaly in middle China, while the contributions of the horizontal transport term to the negative precipitation anomaly are overall comparable to those of the vertical transport term. Specifically, the centers of the horizontal transport term (Fig. 3b, e, h) are close overall to the coast of middle China and the East China Sea, and the overall patterns are to the east of the vertical

transport term (Fig. 3a, d, g). This result implies that the dynamics of the precipitation response may be attributed to changes in different climate systems.

In July, the vertical transport terms (Fig. 4a, d, g) are still the dominant terms for the total sum of the advection terms (Fig. 4c, f, i) and the precipitation responses (Figs. 1d, f, h). However, unlike in June, the horizontal terms (Fig. 4b, e, h) did not show dipole patterns as the vertical terms were all very weak over East Asia. Therefore, we concluded that both the vertical and horizontal advection terms of water vapor contribute to the precipitation responses in June, while only the vertical transport term is important for precipitation responses in July.

We further decompose vertical moisture advection into three components: the first part ($-\langle \bar{\omega} \partial_p q' \rangle$) is the anomalous moisture convergence caused by changes in water vapor content, namely the

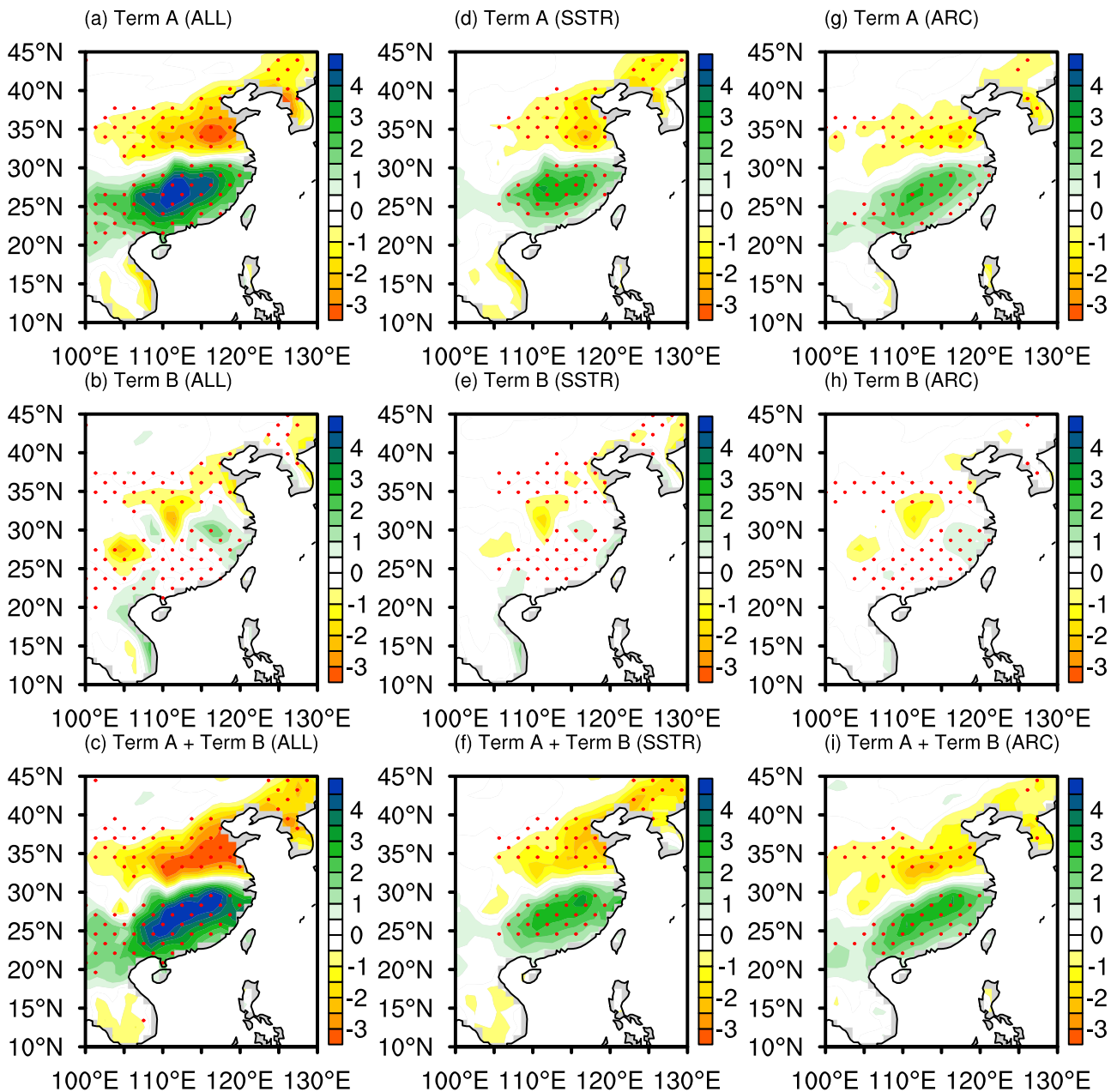


Fig. 4 | Moisture processes driving changes in the precipitation anomaly (July). The vertical transport differences in water vapor ($-\langle\omega\partial_p q\rangle'$, units: mm day^{-1}) responses to ALL (a), SSTR (d) and ARC (g). The horizontal transport differences in water vapor ($-\langle\nabla_h\cdot\nabla_h q\rangle'$, units: mm day^{-1}) responses to ALL (b), SSTR (e) and

ARC (h). The total transport differences in water vapor ($-\langle\omega\partial_p q\rangle' - \langle\nabla_h\cdot\nabla_h q\rangle'$, units: mm day^{-1}) responses to ALL (c), SSTR (f) and ARC (i). Stippling indicates where the multimodel ensemble mean response is significant (90% confidence).

thermally induced anomalous moisture convergence term; the second part ($-\langle\omega'\partial_p q\rangle'$) is the anomalous moisture convergence resulting from changes in atmospheric circulation, namely the dynamically induced anomalous moisture convergence term; and the third part ($-\langle\omega'\partial_p q'\rangle'$) is the nonlinear term. The third part is often negligible and can be ignored. The contribution of the thermal term of vertical water vapor advection to precipitation is small and almost negligible in June and July (Supplementary Figs. 5, 6). The role of the dynamical term dominates the response of precipitation in June and July (Supplementary Figs. 5, 6). Changes in atmospheric circulation in June and July caused differences in precipitation response. To investigate the associated circulation changes and understand the dynamics involved, the atmospheric responses in the three experiments are analyzed in the following sections.

Atmospheric dynamics analysis

According to the moisture budget analysis, the change in atmospheric circulation is the most important trigger for the precipitation response over East Asian land in both June and July. Here, we show the winds and geopotential height responses at 850 hPa and 200 hPa, respectively, for the ALL/SSTR/ARC experiment in Fig. 5 to understand the associated dynamics and differences between June and July. It is clear that the cyclonic shear in middle China, as shown in Fig. 1c, is part of the low-pressure anomaly over Japan in Fig. 5b. At the upper level (Fig. 5a), a strong anticyclonic anomaly is located over southern China and the western Pacific, and a meridional wave-like pattern appears over eastern Eurasia. The convergence in the low level and divergence in the upper level are conducive to vertical motion, favoring increased precipitation over the Yangtze River basin in June. In July (Fig. 5d), the low-level atmospheric responses mainly appear as a strong

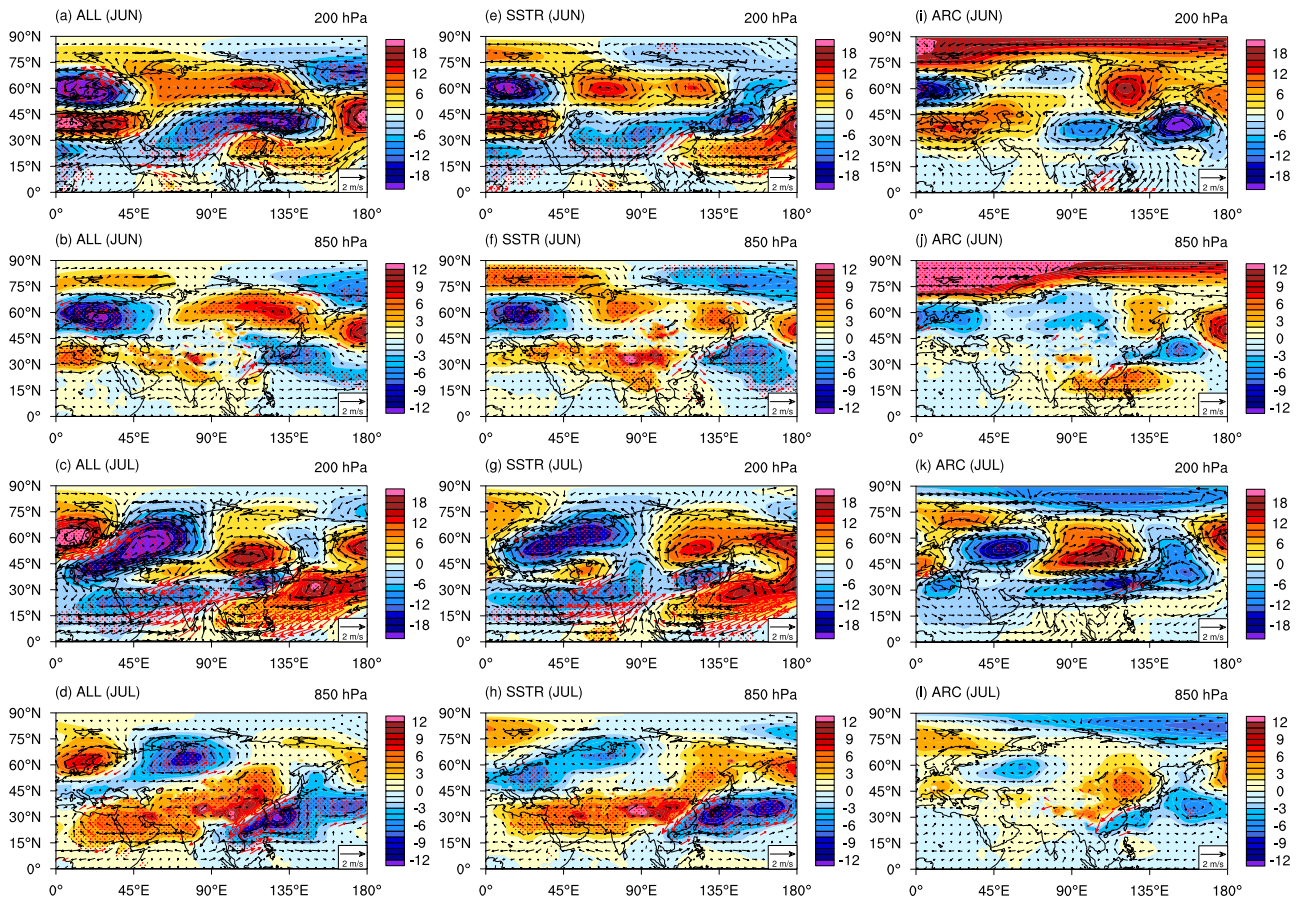


Fig. 5 | Analysis of geopotential height and wind responses. The 200 hPa latitudinal deviation field of geopotential height (shading, units: m) and wind (vector, units: $m s^{-1}$) responses to ALL in June (a) and July (c). The 850 hPa latitudinal deviation field of geopotential height (shading, units: m) and wind (vector, units: $m s^{-1}$) responses to ALL in June (b) and July (d). The 200 hPa latitudinal deviation field of geopotential height (shading, units: m) and wind (vector, units: $m s^{-1}$) responses to SSTR in June (e) and July (g). The 850 hPa latitudinal deviation field of geopotential height (shading, units: m) and wind (vector, units: $m s^{-1}$) responses to SSTR in June (f) and July (h). The 200 hPa geopotential height (shading, units: m) and wind (vector, units: $m s^{-1}$) responses to ARC in June (i) and July (k). The 850 hPa geopotential height (shading, units: m) and wind (vector, units: $m s^{-1}$) responses to ARC in June (j) and July (l). Stippling and red vectors indicate where the multimodel ensemble mean response is significant (90% confidence).

dipole pattern over East Asian land to the western Pacific, with a cyclonic anomaly and low-pressure anomaly from south China to south Japan, which is different from the pattern in June (Fig. 5b). At the upper level (Fig. 5c), a wave-like pattern is very clear over the Eurasian continent, which propagates from the Atlantic Ocean. Moreover, the meridional triple pattern of geopotential height over East Asia tilted to the east of Japan in July compared to the meridional pattern in June. The atmospheric baroclinicity increases over South China in July due to the changes in the vertical shear of circulation, which favors precipitation over South China in July (Fig. 1d).

The contributions of the SST and Arctic sea ice forcing to the changes in circulations are shown in Fig. 5e–l, respectively. In SSTR (Fig. 5e–h), the circulation responses to the changes in SST in both June and July are similar overall to those in ALL (Fig. 5a–d). However, there are still some differences. In June (Fig. 5f), the cyclonic circulation anomaly center and associated low geopotential height are in the mid-latitudes of the Pacific, which are east of the cyclonic circulation center in ALL (Fig. 5b). Therefore, over East Asian land, horizontal cyclonic shear prevails over middle and southern China, which favors local precipitation (Fig. 1e). At the upper level, the wave patterns in the mid-high latitudes in the SSTR (Fig. 5e) are similar overall to those shown in ALL (Fig. 5a), except that the meridional triple pattern over East Asian land in ALL shifted east to the western Pacific Ocean in the SSTR. Therefore, the upper-level westerly anomaly over middle China is weaker in SSTR (Fig. 5e) than in ALL (Fig. 5a). Consequently, the local atmosphere baroclinicity is weaker and the precipitation response is also weaker in SSTR

(Fig. 1e) than in ALL (Fig. 1c). In July, the low-level circulation responses in SSTR (Fig. 5h) are similar overall to those in ALL (Fig. 5d), except that the cyclonic anomaly center over the central Pacific is stronger in SSTR than in ALL, while the horizontal cyclonic shear over South China is weaker in SSTR than in ALL. At the upper level (Fig. 5g), the overall wave pattern in the Northern Hemisphere in SSTR is very similar to that in ALL (Fig. 5c), except that the intensity of the meridional triple pattern over Eastern Eurasia is weaker in SSTR. This result also indicates that the vertical shear of wind over East Asian land is weaker in SSTR than in ALL; consequently, the associated vertical velocity and precipitation response is weaker, but the spatial pattern matches well.

The circulation responses to the Arctic sea ice forcing in the ARC show very different patterns (Figs. 5i–l) compared with those in the ALL and SSTR in both months. In June (Fig. 5j), the low-level circulation shows a strong anticyclone anomaly over the South China Sea and western Pacific. Therefore, southwesterlies prevail over South China and bring more water vapor from the ocean to the Yangtze River basin. In the upper level (Fig. 5i), the wave propagation is quite clear in the mid-high latitudes. There seem to be two propagation paths. One passes through the Barents-Kara Sea (BKS) and propagates to the southeast into the high latitudes of the Eastern Eurasian continent. The other passes through north Africa in the mid-latitudes and propagates zonally to the east of China. Note that over northern China and East Japan, there are two cyclonic anomalies. This structure produces a weak anticyclone in the south and triggers local downward motion

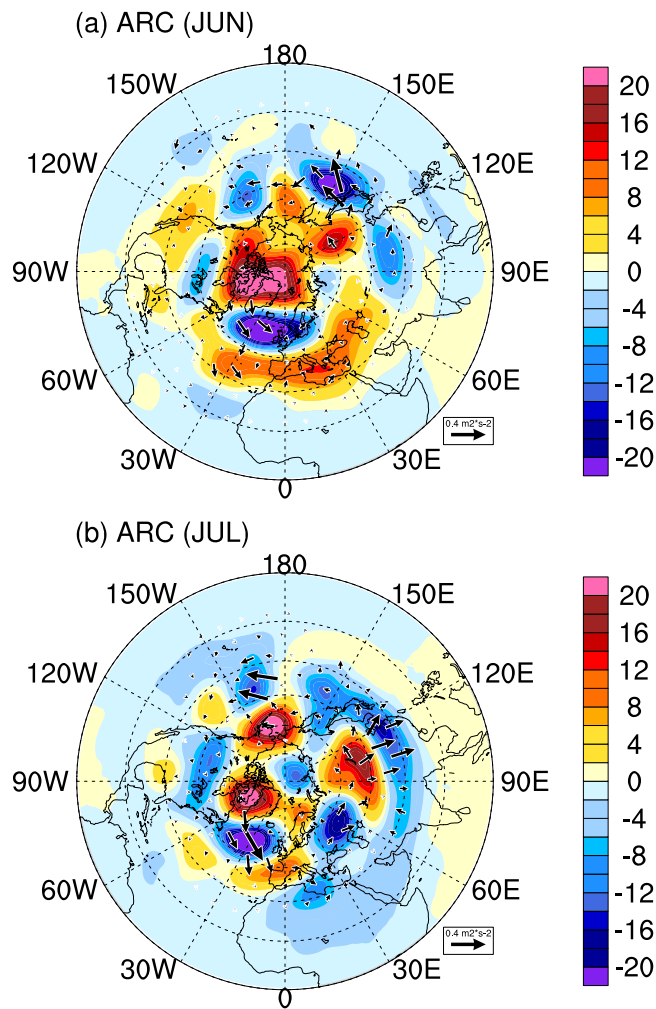


Fig. 6 | Responses of wave-activity flux and geopotential height. The 200 hPa wave-activity flux (vector, units: $\text{m}^2 \text{s}^{-2}$) and 200 hPa geopotential height (shading, units: m) response to ARC in June (a). b is the same as a but in July.

(Supplementary Fig. 7). The upper atmosphere in South China converges and sinks, leading to adiabatic warming, which is conducive to the development of low-level high pressure (Supplementary Fig. 7; Fig. 5j). Consequently, it intensifies the low-level anticyclonic anomaly, which is crucial for the increase in precipitation in the Yangtze River basin (Fig. 1g).

In July (Fig. 5k, l), the circulation responses are different from those in June. At low levels (Fig. 5l), the geopotential height anomalies mainly show a zonal dipole pattern over eastern China and the western Pacific. This pattern is very similar to that in ALL (Fig. 5d) and SSTR (Fig. 5h), but the intensity is much weaker. In the upper level (Fig. 5k), the wave pattern mainly shows a meridional triple pattern over the Eastern Eurasian continent. The negative geopotential height anomaly over middle China produces a strong westerly on its south and enhances the local baroclinicity in south China, which favors the precipitation increase. In summary, the circulation responses to the Arctic sea ice forcing in June and July are quite different, which may be connected with the different sea ice losses in these two months (Supplementary Fig. 8). However, the model results show that the trigger and propagation of the Rossby wave in the upper level is the most important way to modulate the Arctic sea ice forcing on the East Asian circulation patterns.

To further quantitatively identify the wave propagation in the middle and upper layers induced by different sea ice forcings, we calculated the associated wave activity fluxes (WAFs) in the ARC case. The detailed calculation of the WAF is shown in Eq. 6, following Takaya and Nakamura⁶⁶,

which has been widely used in climate diagnostics. In June (Fig. 6a), since the Arctic sea ice mainly decreases in the BKS, the local geopotential height anomaly in the upper layer shows a strong meridional triple pattern from the polar region to the Atlantic Ocean. The WAFs show two clear branches originating from this triple pattern at both high and mid-latitudes. One branch originates from the negative geopotential height center over southern Greenland and propagates zonally to the high latitudes of eastern Eurasia associated with a strong positive geopotential height anomaly. The other branch originates from the positive center over the Atlantic Ocean and propagates zonally to the mid-latitudes of the western Pacific associated with the two negative centers. In July (Fig. 6b), the WAF shows a very different pattern from that in June. The WAF is quite strong over the eastern Eurasian continent from high latitudes to mid-latitudes. The above analysis indicates that the location of Arctic sea ice loss is crucial for stationary wave changes in the mid-high latitudes of the Northern Hemisphere and is also important for precipitation distributions in East Asia at lower latitudes. The Linear Baroclinic Model (LBM) shows similar results. In June, the reduction of sea ice in the Barents Sea is accompanied by anomalous geopotential heights that propagate along the westerlies to East Asia, resulting in negative geopotential height anomalies over eastern China (Supplementary Table 2; Supplementary Fig. 9). In July, in addition to the reduction of sea ice in the Barents Sea, the decline of sea ice along the Russian northern coastline also occurs, accompanied by anomalous geopotential heights that are conveyed along the westerlies to East Asia, leading to anomalous geopotential height patterns over eastern China (Supplementary Table 2; Supplementary Fig. 10). The anomalous geopotential height centers in the LBM experiments exhibit some discrepancies with those in the PAMIP experiments, which may be attributed to the reduction of sea ice in other regions and the effects of nonlinear interactions.

The westerly jet in the Northern Hemisphere acts as the wave guide for the propagation of the Rossby wave^{67–70}. The changes in the westerly jet under global warming will influence the stationary wave pattern in the mid-high latitudes. Many previous studies have noted that Arctic amplification and the associated Arctic sea ice loss warm the underlying surface and upper level air, thus weakening the large-scale atmospheric meridional thermal gradient from the equator to the polar region. Consequently, the subtropical atmosphere baroclinicity is weakened, and the westerly jet is also weakened, especially in the boreal winter season^{55,71,72}. To understand the responses of the westerly jet and meridional thermal structure to the SST and SIC forcing, we show the responses of the zonal wind at 200 hPa in the three experiments (Fig. 7). In June, the zonal wind response shows a clear decrease over northern China and an increase in middle China in ALL (Fig. 7a), indicating that the westerly jet is weakened and shifts south over East Asia. This pattern is very similar to that in the SSTR (Fig. 7b), while the zonal wind response in the ARC is much weaker (Fig. 7c). This result means that the contributions of Arctic sea ice loss to the weakening of the westerly jet in June are very limited.

In July (Fig. 7d), the zonal wind response is slightly different from that in June for the ALL case. The zonal wind increases in middle and south China but decreases in northern China. Moreover, the wind responses in SSTR are very similar to those in ALL (Fig. 7e), when the wind responses are relatively weak in ARC in July (Fig. 7f), although they are slightly stronger than those in June. The overall wind responses in the ARC and SSTR are similar between June and July, but the locations of the wind anomaly are slightly different over East Asia, which is crucial for the location of the precipitation system. Furthermore, it also indicates that the warmer SST in middle and high latitudes is crucial for the weakness of the westerly jet under global warming, when the contributions from Arctic sea ice loss are limited. We further examine the cross-section of the air temperature difference and the associated changes in zonal wind for the zonal mean of 105–120°E in Fig. 8. Clearly, the air temperature warms at the mid-high level from the tropics to the subtropics and warms at the mid-low level within the latitude band between 40–70°N in ALL and SSTR in both June (Fig. 8a, b) and July (Fig. 8d, e). The warming over mid-high latitudes weakens the meridional thermal

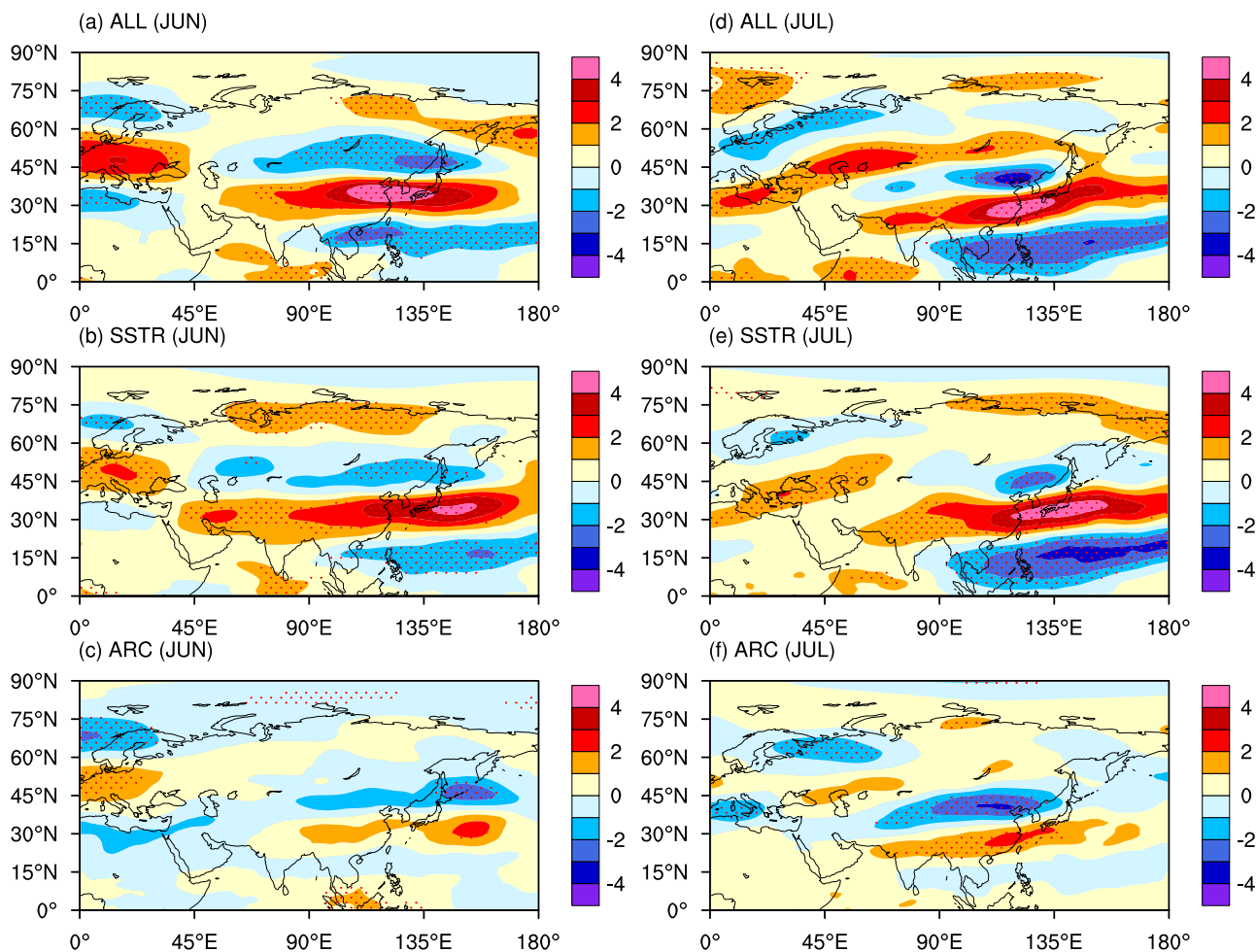


Fig. 7 | The 200 hPa zonal wind responses. The 200 hPa zonal wind (units: m s^{-1}) responses to ALL (a), SSTR (b) and ARC (c) in June. The 200 hPa zonal wind (units: m s^{-1}) responses to ALL (d), SSTR (e) and ARC (f) in July. Stippling indicates where the multimodel ensemble mean response is significant (90% confidence).

gradient and leads to a reduction in the wind speed in the northern part of the westerly jet and an increase in the wind speed in the southern part of the westerly jet. Notably, the zonal mean responses of the air temperature difference and zonal wind are both weak in the ARC in June and July. Therefore, the contributions of Arctic sea ice loss to the large-scale meridional thermal contrast are very limited. The observed weakness and southward shift of the westerly jet should be attributed to the warming of the global SST and not Arctic amplification.

Discussion

In this study, the role of Arctic sea ice loss and SST increase on EASM climate changes under a global warming background is investigated by analyzing large ensemble simulations from CMIP6 PAMIP multimodel experiments. The results highlight that Arctic sea ice loss plays an important role in the changes in EASM precipitation multidecadal trends, which is comparable to the influences of SST distributions in June and July. However, the physical mechanisms of Arctic sea ice loss on the changes in precipitation over East Asia are quite different between June and July.

For simplicity, we summarized the relative physical process using the schematic diagram in Fig. 9. In June (Fig. 9a), the Arctic sea ice mainly decreases in the BKS, and the perturbations of sea ice loss lead to an upper level circulation anomaly, which appears as a stationary wave of a strong triple pattern over the Atlantic sector and propagates through two pathways into the East Eurasia continent. Two cyclonic anomaly centers are located over middle China and the northwest Pacific. This pattern favors a

weak anticyclone in the upper level and forms a descending motion over the South China Sea and western Pacific. Therefore, it enhances the low-level anticyclonic anomaly, which brings more water vapor from the ocean into the Yangtze River basin and leads to more precipitation and forms the meridional triple rainfall pattern. In July (Fig. 9b), except for the decrease in sea ice in the BKS, the sea ice also decreases along the northern coast of Russia. The decrease in sea ice produces a strong meridional triple wave pattern over the Eastern Eurasian continent and weakens the atmospheric baroclinicity over middle China; thus, the monsoon circulation is weakened and produces a classical “southern China flood and northern China drought” pattern.

Although Arctic sea ice loss is important for EASM multidecadal changes, it is still not the dominant factor. The SST warming over middle and high latitudes plays an important role in weakening the large-scale thermal contrast and the westerly jet in the Northern Hemisphere, which has a large impact on Rossby wave propagation in the subtropics. Moreover, SST warming over the northwest Pacific produces low-level cyclonic circulation, which favors monsoon precipitation. We want to emphasize that although many previous studies have proposed that anthropogenic aerosols have been the source of EASM precipitation increases in recent decades^{73,74}, the combined effect of SST warming and Arctic sea ice loss plays a more important role in the changes in the location and vertical structure of the monsoon precipitation system over East Asia. The quantitative estimations of the relative contributions of these external forcings to the changes in the EASM need more study. Additionally, since the PAMIP experiments used in this study are all based on AMIP-type runs, the air-sea interactions

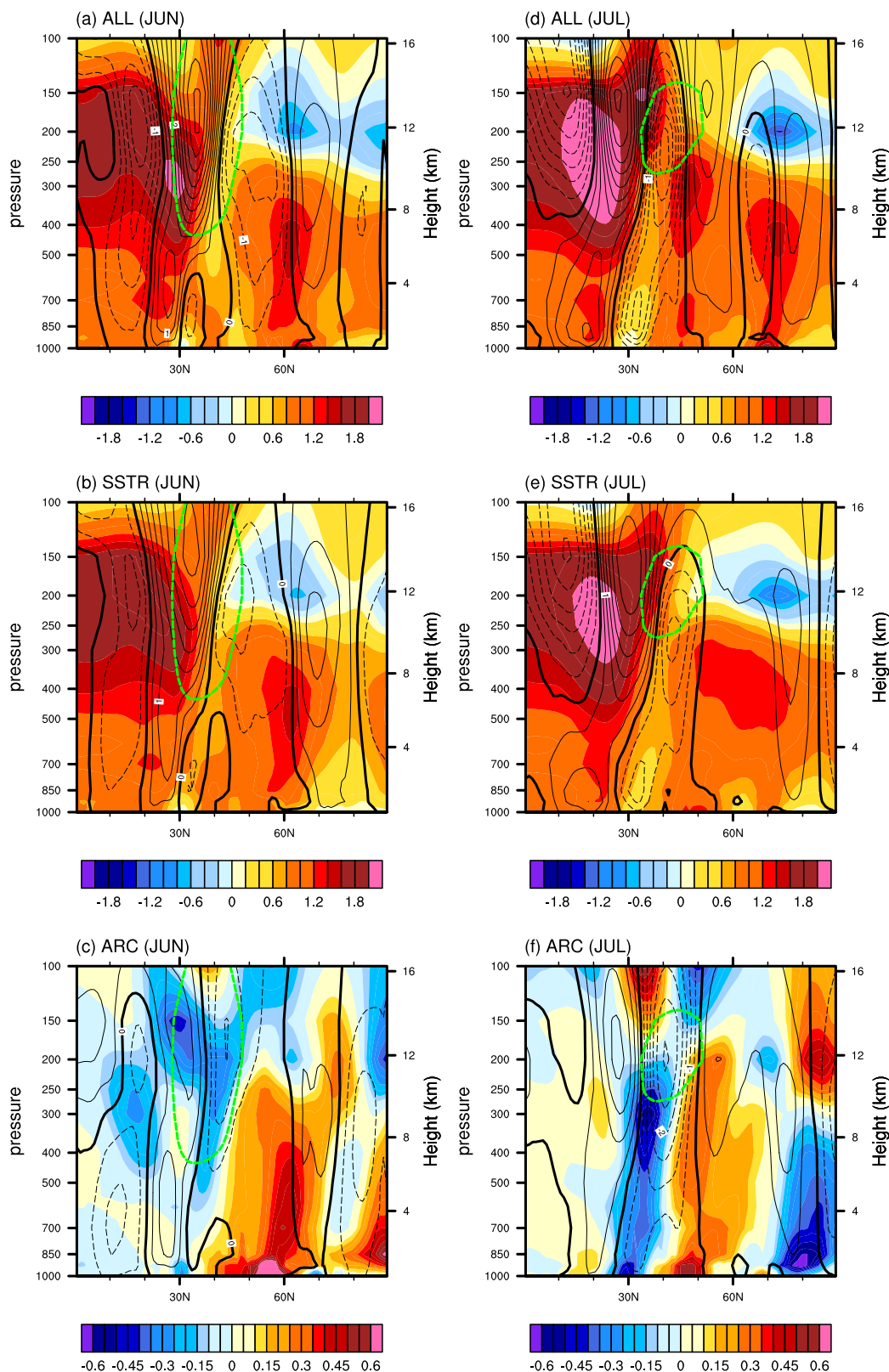


Fig. 8 | The temperature and zonal wind responses. The temperature (shading, units: K) and zonal wind (contour, units: m s^{-1}) averaged over 105°E – 120°E responses to ALL (a, d), SSTR (b, e) and ARC (c, f) in June (a, b, c) and July (d, e, f), respectively.

The green dashed line indicates the position of the jet (more than 12 m s^{-1}) in pdSST-pdSIC (a–f).

induced by Arctic sea ice loss cannot be investigated. Therefore, air-sea coupled models must be used in the future to understand the involved air-sea interactions, which are important for the formation of and changes in the Asian monsoon system.

Methods

Observational and reanalysis datasets

The following observational and reanalysis datasets are used in this study: (i) rainfall datasets from the Global Precipitation Climatology

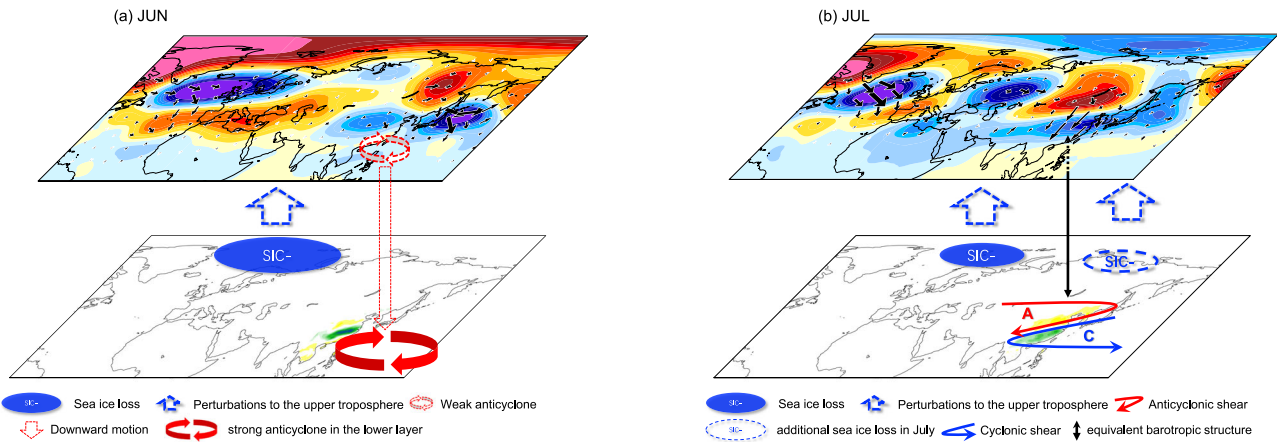


Fig. 9 | Mechanisms of East Asian summer precipitation responses. Mechanisms of East Asian summer precipitation responses to Arctic sea ice loss based on the ARC experiment in (a) June and (b) July.

Centre ($1^\circ \times 1^\circ$; GPCC v7, 1901-2018)⁷⁵ and (ii) wind datasets from the European Center for Medium-Range Weather Forecast (ECMWF) and the ERA5 Reanalysis ($0.25^\circ \times 0.25^\circ$; ERA5, 1950-2010)⁷⁶.

PAMIP experiment in CMIP6

The experiments used are from the Polar Amplification Model Intercomparison Project (PAMIP)⁵⁴. As shown in Table 1, PAMIP experiment 1 simulates the present-day climate using global atmosphere models constrained at the surface by present-day estimates of sea surface temperature (SST) and sea ice concentration (SIC). The present-day SST (pdSST) and SIC (pdSIC) were obtained from the observations, using the 1979–2008 climatology from the Hadley Centre Sea Ice and Sea Surface Temperature dataset (HadISST)⁷⁷. The climatological SSTs and SICs are used for the PAMIP simulations. The No. 2 experimental group, piSST-piSIC, was forced by pre-industrial SST and SIC. The pre-industrial SST (piSST) and SIC (piSIC) were obtained from the ensemble of 31 historical CMIP5 model outputs, but with estimated global warming indices removed for the 1979–2008 period. No. 3 is the same as No. 1 except that SST is replaced with pre-industrial values. No. 4 is the same as No. 1 except that Arctic SIC is replaced with pre-industrial values. Through construction, the difference between No. 1 and No. 2 provides the simulated response to SST rise and sea ice loss (ALL) (No. 5). As above, No. 6 can represent the response to SST rise (SSTR), and No. 7 can represent the response to Arctic SIC loss (ARC). The PAMIP model only integrated for 14 months, starts from April 1, 2000. We analyze the results from 6 models, each with at least 100 ensemble members (Supplementary Table 1) and forced with the same SSTs and SICs. Details of the number of model experiments are shown in Supplementary Table 1, e.g., HadGEM3-GC31-MM provides 149 ensemble members of piSST-piSIC, 150 ensemble members of piSST-pdSIC, 300 ensemble members of pdSST-piArcSIC, and 300 ensemble members of pdSST-pdSIC. We used all the available 6 models with more than 700 ensemble members for the analysis of the results. All data were regridded to the resolution of the GPCC datasets (1° latitude by 1° longitude) before use.

Statistical methods

The pattern correlation is the Pearson product-moment coefficient of linear correlation between two variables that are the values of the same variables at corresponding locations on two different maps. The pattern correlation was used to select the top 100 ensemble members whose precipitation responses to ALL were consistent with GPCC precipitation trends in June (July) (Supplementary Table 3). We used a t-test to test the statistical significance

of the response to ALL/SSTR/ARC. The t-test formula is defined as follows:

$$t = \frac{\bar{x}_1 - \bar{x}_2}{\sqrt{\frac{s_1^2}{N_1} + \frac{s_2^2}{N_2}}} \tag{1}$$

where \bar{x}_1 , s_1 and N_1 represent the mean, variance, and number of samples, respectively. \bar{x}_2 , s_2 and N_2 are the same as above.

Observation constraint

To study the summer precipitation distribution in East Asia under the influence of global warming, we firstly evaluated the model’s simulation ability on capturing the basic responses of EASM to SST and SIC (as shown in Table 1, No.5 ALL: pdSST-pdSIC (NO.1) minus piSST-piSIC (NO.2)) with all the available model ensemble members (749 ensemble members) and then the first high skill 100 ensemble members are selected. These ensemble members are shown in Supplementary Table 3.

To implement this method, the spatial correlation coefficients between the spatial distribution of precipitation response to ALL and the spatial distribution of interdecadal precipitation trends in the GPCC are calculated. Next, the spatial correlation coefficients of all ensemble members were ranked and filtered to obtain the first 100 ensemble members with higher skills. These members were considered the most reliable for characterizing the observed interdecadal trend distribution of summer precipitation in East Asia. Finally, the analysis was based on the ensemble average of these 100 ensemble members, which provided a more accurate and reliable estimate of the distribution of summer precipitation in East Asia. All the available ensemble members of PAMIP were used. The selected ensemble members are the members which have good skill on capturing the observed climate trend of precipitation over East Asia, and by using this kind of selection, the multi-model biases can be removed to some extent. This method of observation constraint helps to improve the accuracy of climate models and provides a better understanding of how global warming affects summer precipitation in East Asia.

Moisture budget diagnostics

We applied moisture budget diagnostics to investigate the physical processes driving the changes in precipitation^{63–65}. In a climate state, precipitation (P) is balanced by evaporation (E) and vertical ($-\langle \omega \partial_p q \rangle$) and horizontal ($-\langle \mathbf{V}_h \cdot \nabla_h q \rangle$) moisture advection that are related to low-level convergence and horizontal winds, respectively.

$$P = E - \langle \omega \partial_p q \rangle - \langle \mathbf{V}_h \cdot \nabla_h q \rangle + \delta \tag{2}$$

where q is the specific humidity, ω is the vertical velocity, \mathbf{V}_h is the horizontal wind vector, δ is the residual, and $\langle \cdot \rangle = \frac{1}{g} \int_{p_s}^{p_t} \cdot dp$ denotes the vertical integral throughout the troposphere. This equation can also characterize the response of each term to ALL/SSTR/ARC as follows:

$$P' = E' - \langle \omega \partial_p q' \rangle - \langle \mathbf{V}_h \cdot \nabla_h q' \rangle + \delta' \quad (3)$$

The response of the vertical moisture advection ($-\langle \omega \partial_p q' \rangle$) can be further divided into three terms: the first part ($-\langle \bar{\omega} \partial_p q' \rangle$), the second part ($-\langle \omega' \partial_p \bar{q} \rangle$) and the third part ($-\langle \omega' \partial_p q' \rangle$)^{78,79}.

$$-\langle \omega \partial_p q' \rangle = -\langle \bar{\omega} \partial_p \bar{q}' \rangle - \langle \omega' \partial_p \bar{q}' \rangle - \langle \omega' \partial_p q' \rangle \quad (4)$$

where q is the specific humidity, ω is the vertical velocity, and $\langle \cdot \rangle = \frac{1}{g} \int_{p_s}^{p_t} \cdot dp$ denotes the vertical integral throughout the troposphere. “ $\bar{\omega}$ ” denotes the vertical velocity in the pdSST-pdSIC experiment, and “ q' ” denotes the specific humidity’s response to ALL/SSTR/ARC.

Thermal wind

The geostrophic balance between the pressure gradient and Coriolis forces, combined with the hydrostatic equation, leads to the thermal wind relationship, showing that a reduction in the meridional temperature gradient as the Arctic warms is accompanied by a decrease in vertical wind shear.

$$f \frac{\partial u}{\partial p} = \frac{R}{ap} \frac{\partial T}{\partial \varphi} \quad (5)$$

where u, T, p , and φ are the zonal wind, temperature, pressure and latitude, respectively; f is the Coriolis parameter; a is the radius of the Earth; and R is the gas constant.

Wave activity flux

The WAF derived by Takaya and Nakamura (hereafter TN01) is used to measure the wave propagation⁶⁶. Its horizontal components in pressure coordinates are obtained as follows:

$$W = \frac{pcos\varphi}{2|U|} \cdot \begin{cases} \frac{U}{a^2 \cos^2 \varphi} \left[\left(\frac{\partial \psi'}{\partial \lambda} \right)^2 - \psi' \frac{\partial^2 \psi'}{\partial \lambda^2} \right] + \frac{V}{a^2 \cos \varphi} \left[\left(\frac{\partial \psi'}{\partial \lambda} \frac{\partial \psi'}{\partial \varphi} \right) - \psi' \frac{\partial^2 \psi'}{\partial \lambda \partial \varphi} \right] \\ \frac{U}{a^2 \cos \varphi} \left[\left(\frac{\partial \psi'}{\partial \lambda} \frac{\partial \psi'}{\partial \varphi} \right) - \psi' \frac{\partial^2 \psi'}{\partial \lambda \partial \varphi} \right] + \frac{V}{a^2} \left[\left(\frac{\partial \psi'}{\partial \varphi} \right)^2 - \psi' \frac{\partial^2 \psi'}{\partial \varphi^2} \right] \end{cases} \quad (6)$$

The quantity $|U|$ denotes the magnitude of the wind in the pdSST-pdSIC experiment. U and V represent the zonal and meridional wind, respectively. ψ is the stream function, and p is the normalized pressure (pressure/1000 hPa). a, λ and φ represent the radius of the Earth, longitude and latitude, respectively. A superscript with a prime characterizes the variable’s response to ALL/SSTR/ARC.

Data availability

The GPCC data are downloaded from <https://psl.noaa.gov/data/gridded/data/gpcc.html>. The ERA5 data are available at <https://cds.climate.copernicus.eu/cdsapp#!/dataset/reanalysis-era5-pressure-levels?tab=overview>. The PAMIP data are available at <https://aims2.llnl.gov/search/cmip6/>.

Code availability

The codes for creating the figures and analyses were written in NCAR Command Language Version 6.6. The source codes for the analysis of this study are available from the corresponding author upon reasonable request.

Received: 14 November 2023; Accepted: 9 July 2024;
Published online: 24 July 2024

References

1. Barlow, M., Cullen, H. & Lyon, B. Drought in Central and Southwest Asia: La Niña, the Warm Pool, and Indian Ocean Precipitation. *J. Clim.* **15**, 697–700 (2002).
2. Chang, C.-P., Zhang, Y. & Li, T. Interannual and Interdecadal Variations of the East Asian Summer Monsoon and Tropical Pacific SSTs. Part I: Roles of the Subtropical Ridge. *J. Clim.* **13**, 4310–4325 (2000).
3. Gong, D.-Y. & Ho, C.-H. Shift in the summer rainfall over the Yangtze River valley in the late 1970s. *Geophys. Res. Lett.* **29**, 78–71–78–74 (2002).
4. Gong, D.-Y. & Ho, C.-H. Arctic oscillation signals in the East Asian summer monsoon. *J. Geophys. Res. Atmos.* **108**, 4066 (2003).
5. He, B. et al. Model sensitivity of Tibetan Plateau surface potential vorticity and the Asian summer monsoon system to Asian orographic perturbation in FGOALS-f2. *Fundam. Res.* <https://doi.org/10.1016/j.fmre.2023.08.013> (2023).
6. He, B., Liu, Y., Wu, G., Wang, Z. & Bao, Q. The role of air–sea interactions in regulating the thermal effect of the Tibetan–Iranian Plateau on the Asian summer monsoon. *Clim. Dyn.* **52**, 4227–4245 (2019).
7. He, B., Sheng, C., Wu, G., Liu, Y. & Tang, Y. Quantification of seasonal and interannual variations of the Tibetan Plateau surface thermodynamic forcing based on the potential vorticity. *Geophys. Res. Lett.* **49**, e2021GL097222 (2022).
8. Hu, W., Duan, A., Li, Y. & He, B. The intraseasonal oscillation of Eastern Tibetan plateau precipitation in response to the summer Eurasian Wave Train. *J. Clim.* **29**, 7215–7230 (2016).
9. Hu, W., She, D., Xia, J., He, B. & Hu, C. Dominant patterns of dryness/wetness variability in the Huang-Huai-Hai River Basin and its relationship with multiscale climate oscillations. *Atmos. Res.* **247**, 105148 (2021).
10. Hu, Z.-Z. Interdecadal variability of summer climate over East Asia and its association with 500 hPa height and global sea surface temperature. *J. Geophys. Res. Atmos.* **102**, 19403–19412 (1997).
11. Huang, R., Chen, J. & Huang, G. Characteristics and variations of the East Asian monsoon system and its impacts on climate disasters in China. *Adv. Atmos. Sci.* **24**, 993–1023 (2007).
12. Ding, Y. & Chan, J. C. L. The East Asian summer monsoon: an overview. *Meteorol. Atmos. Phys.* **89**, 117–142 (2005).
13. Yu, R. & Zhou, T. Seasonality and three-dimensional structure of interdecadal change in the East Asian Monsoon. *J. Clim.* **20**, 5344–5355 (2007).
14. Zhou, T., Gong, D. & Li, J. Detecting and understanding the multi-decadal variability of the East Asian summer monsoon—Recent progress and state of affairs. *Meteorol. Z.* **18**, 455–467 (2009).
15. Menon, S., Hansen, J., Nazarenko, L. & Luo, Y. Climate effects of black carbon aerosols in China and India. *Science* **297**, 2250–2253 (2002).
16. Huang, Y., Dickinson, R. E. & Chameides, W. L. Impact of aerosol indirect effect on surface temperature over East Asia. *Proc. Natl Acad. Sci. USA* **103**, 4371–4376 (2006).
17. Li, L., Wang, B. & Zhou, T. Contributions of natural and anthropogenic forcings to the summer cooling over eastern China: An AGCM study. *Geophys. Res. Lett.* **34**, <https://doi.org/10.1029/2007GL030541> (2007).
18. Ramanathan, V. & Carmichael, G. Global and regional climate changes due to black carbon. *Nat. Geosci.* **1**, 221–227 (2008).
19. Rosenfeld, D. et al. Flood or drought: how do aerosols affect precipitation? *Science* **321**, 1309–1313 (2008).
20. Wu, B., Zhang, R., Wang, B. & D’Arrigo, R. On the association between spring Arctic sea ice concentration and Chinese summer rainfall. *Geophys. Res. Lett.* **36**, <https://doi.org/10.1029/2009GL037299> (2009).

21. Song, F., Zhou, T. & Qian, Y. Responses of East Asian summer monsoon to natural and anthropogenic forcings in the 17 latest CMIP5 models. *Geophys. Res. Lett.* **41**, 596–603 (2014).
22. Li, Z. et al. Aerosol and monsoon climate interactions over Asia. *Rev. Geophys.* **54**, 866–929 (2016).
23. Wu, G. et al. Advances in studying interactions between aerosols and monsoon in China. *Sci. China Earth Sci.* **59**, 1–16 (2016).
24. Hu, Z.-Z., Yang, S. & Wu, R. Long-term climate variations in China and global warming signals. *J. Geophys. Res. Atmos.* **108**, <https://doi.org/10.1029/2003JD003651> (2003).
25. Held, I. M. & Soden, B. J. Robust responses of the hydrological cycle to global warming. *J. Clim.* **19**, 5686–5699 (2006).
26. Li, J., Wu, Z., Jiang, Z. & He, J. Can global warming strengthen the East Asian Summer Monsoon? *J. Clim.* **23**, 6696–6705 (2010).
27. He, B. et al. Influences of external forcing changes on the summer cooling trend over East Asia. *Clim. Change* **117**, 829–841 (2013).
28. Holland, M. M. & Bitz, C. M. Polar amplification of climate change in coupled models. *Clim. Dyn.* **21**, 221–232 (2003).
29. Screen, J. A. & Simmonds, I. The central role of diminishing sea ice in recent Arctic temperature amplification. *Nature* **464**, 1334–1337 (2010).
30. Screen, J. A., Deser, C. & Simmonds, I. Local and remote controls on observed Arctic warming. *Geophys. Res. Lett.* **39**, <https://doi.org/10.1029/2012GL051598> (2012).
31. Cohen, J. et al. Recent Arctic amplification and extreme mid-latitude weather. *Nat. Geosci.* **7**, 627–637 (2014).
32. Mori, M., Watanabe, M., Shiogama, H., Inoue, J. & Kimoto, M. Robust Arctic sea-ice influence on the frequent Eurasian cold winters in past decades. *Nat. Geosci.* **7**, 869–873 (2014).
33. Screen, J. A., Deser, C., Simmonds, I. & Tomas, R. Atmospheric impacts of Arctic sea-ice loss, 1979–2009: separating forced change from atmospheric internal variability. *Clim. Dyn.* **43**, 333–344 (2014).
34. Gramling, C. Arctic impact. *Science* **347**, 818–821 (2015).
35. Overland, J. et al. The melting Arctic and midlatitude weather patterns: are they connected? *J. Clim.* **28**, 7917–7932 (2015).
36. Shepherd, T. G. Effects of a warming Arctic. *Science* **353**, 989–990 (2016).
37. Zhang, P. et al. A stratospheric pathway linking a colder Siberia to Barents-Kara Sea sea ice loss. *Sci. Adv.* **4**, eaat6025 (2018).
38. Dai, A., Luo, D., Song, M. & Liu, J. Arctic amplification is caused by sea-ice loss under increasing CO₂. *Nat. Commun.* **10**, 121 (2019).
39. Mori, M., Kosaka, Y., Watanabe, M., Nakamura, H. & Kimoto, M. A reconciled estimate of the influence of Arctic sea-ice loss on recent Eurasian cooling. *Nat. Clim. Change* **9**, 123–129 (2019).
40. Francis, J. A. & Vavrus, S. J. Evidence linking Arctic amplification to extreme weather in mid-latitudes. *Geophys. Res. Lett.* **39**, <https://doi.org/10.1029/2012GL051000> (2012).
41. Liu, J., Curry, J. A., Wang, H., Song, M. & Horton, R. M. Impact of declining Arctic sea ice on winter snowfall. *Proc. Natl Acad. Sci.* **109**, 4074–4079 (2012).
42. Kug, J.-S. et al. Two distinct influences of Arctic warming on cold winters over North America and East Asia. *Nat. Geosci.* **8**, 759–762 (2015).
43. Cohen, J. et al. Divergent consensus on Arctic amplification influence on midlatitude severe winter weather. *Nat. Clim. Change* **10**, 20–29 (2020).
44. Serreze, M. C. & Francis, J. A. The Arctic amplification debate. *Clim. Change* **76**, 241–264 (2006).
45. Kim, B.-M. et al. Weakening of the stratospheric polar vortex by Arctic sea-ice loss. *Nat. Commun.* **5**, 4646 (2014).
46. Blackport, R. & Kushner, P. J. The transient and equilibrium climate response to rapid summertime sea ice loss in CCSM4. *J. Clim.* **29**, 401–417 (2016).
47. McCusker, K. E., Fyfe, J. C. & Sigmond, M. Twenty-five winters of unexpected Eurasian cooling unlikely due to Arctic sea-ice loss. *Nat. Geosci.* **9**, 838–842 (2016).
48. Screen, J. A. Simulated atmospheric response to regional and Pan-Arctic sea ice loss. *J. Clim.* **30**, 3945–3962 (2017).
49. Dai, A. & Song, M. Little influence of Arctic amplification on mid-latitude climate. *Nat. Clim. Change* **10**, 231–237 (2020).
50. Murphy, J. M. et al. Quantification of modelling uncertainties in a large ensemble of climate change simulations. *Nature* **430**, 768–772 (2004).
51. Miliuski, S., Maher, N. & Olonscheck, D. How large does a large ensemble need to be? *Earth Syst. Dyn.* **11**, 885–901 (2020).
52. Zhang, X. et al. Evaluation of the seasonality and spatial aspects of the Southern Annular Mode in CMIP6 models. *Int. J. Climatol.* **42**, 3820–3837 (2022).
53. Eyring, V. et al. Overview of the Coupled Model Intercomparison Project Phase 6 (CMIP6) experimental design and organization. *Geosci. Model Dev.* **9**, 1937–1958 (2016).
54. Smith, D. M. et al. The Polar Amplification Model Intercomparison Project (PAMIP) contribution to CMIP6: investigating the causes and consequences of polar amplification. *Geosci. Model Dev.* **12**, 1139–1164 (2019).
55. Smith, D. M. et al. Robust but weak winter atmospheric circulation response to future Arctic sea ice loss. *Nat. Commun.* **13**, 1–15 (2022).
56. Guo, D. et al. Mechanism on how the spring Arctic sea ice impacts the East Asian summer monsoon. *Theor. Appl. Climatol.* **115**, 107–119 (2014).
57. He, S., Gao, Y., Furevik, T., Wang, H. & Li, F. Teleconnection between sea ice in the Barents Sea in June and the Silk Road, Pacific–Japan and East Asian rainfall patterns in August. *Adv. Atmos. Sci.* **35**, 52–64 (2018).
58. Zhao, P., Zhang, X., Zhou, X., Ikeda, M. & Yin, Y. The sea ice extent anomaly in the North Pacific and its impact on the East Asian Summer Monsoon Rainfall. *J. Clim.* **17**, 3434–3447 (2004).
59. Masson-Delmotte, V. et al. Climate change 2021: the physical science basis. *Contribution of working group I to the sixth assessment report of the intergovernmental panel on climate change*. (Cambridge University Press, 2021).
60. Kosaka, Y. & Xie, S.-P. Recent global-warming hiatus tied to equatorial Pacific surface cooling. *Nature* **501**, 403–407 (2013).
61. Yan, X.-H. et al. The global warming hiatus: Slowdown or redistribution? *Earth's Future* **4**, 472–482 (2016).
62. Medhaug, I., Stolpe, M. B., Fischer, E. M. & Knutti, R. Reconciling controversies about the ‘global warming hiatus’. *Nature* **545**, 41–47 (2017).
63. Peng, D., Zhou, T., Zhang, L. & Wu, B. Human contribution to the increasing summer precipitation in Central Asia from 1961 to 2013. *J. Clim.* **31**, 8005–8021 (2018).
64. Shi, J. & Yan, Q. Evolution of the Asian–African monsoonal precipitation over the last 21 kyr and the Associated Dynamic Mechanisms. *J. Clim.* **32**, 6551–6569 (2019).
65. Zhang, W. et al. Increasing precipitation variability on daily-to-multiyear time scales in a warmer world. *Sci. Adv.* **7**, eabf8021 (2021).
66. Takaya, K. & Nakamura, H. A formulation of a phase-independent wave-activity flux for stationary and migratory quasigeostrophic eddies on a zonally varying basic flow. *J. Atmos. Sci.* **58**, 608–627 (2001).
67. Ambrizzi, T., Hoskins, B. J. & Hsu, H.-H. Rossby wave propagation and teleconnection patterns in the Austral Winter. *J. Atmos. Sci.* **52**, 3661–3672 (1995).
68. Ambrizzi, T. & Hoskins, B. J. Stationary rossby-wave propagation in a baroclinic atmosphere. *Q. J. R. Meteorol. Soc.* **123**, 919–928 (1997).
69. Ding, F. & Li, C. Subtropical westerly jet waveguide and winter persistent heavy rainfall in south China. *J. Geophys. Res. Atmos.* **122**, 7385–7400 (2017).
70. An, X. et al. The combined effect of two westerly jet waveguides on heavy haze in the North China Plain in November and December 2015. *Atmos. Chem. Phys.* **20**, 4667–4680 (2020).
71. Deser, C., Sun, L., Tomas, R. A. & Screen, J. Does ocean coupling matter for the northern extratropical response to projected Arctic sea ice loss? *Geophys. Res. Lett.* **43**, 2149–2157 (2016).

72. Screen, J. A. et al. Consistency and discrepancy in the atmospheric response to Arctic sea-ice loss across climate models. *Nat. Geosci.* **11**, 155–163 (2018).
73. Kim, M. J., Yeh, S.-W. & Park, R. J. Effects of sulfate aerosol forcing on East Asian summer monsoon for 1985–2010. *Geophys. Res. Lett.* **43**, 1364–1372 (2016).
74. Tian, F., Dong, B., Robson, J. & Sutton, R. Forced decadal changes in the East Asian summer monsoon: the roles of greenhouse gases and anthropogenic aerosols. *Clim. Dyn.* **51**, 3699–3715 (2018).
75. Schneider, U. et al. GPCC's new land surface precipitation climatology based on quality-controlled in situ data and its role in quantifying the global water cycle. *Theor. Appl. Climatol.* **115**, 15–40 (2014).
76. Hersbach, H. et al. The ERA5 global reanalysis. *Q. J. R. Meteorol. Soc.* **146**, 1999–2049 (2020).
77. Rayner, N. A. et al. Global analyses of sea surface temperature, sea ice, and night marine air temperature since the late nineteenth century. *J. Geophys. Res. Atmos.* **108**, <https://doi.org/10.1029/2002JD002670> (2003).
78. Akinsanola, A. A. & Zhou, W. Dynamic and thermodynamic factors controlling increasing summer monsoon rainfall over the West African Sahel. *Clim. Dyn.* **52**, 4501–4514 (2019).
79. Chou, C. & Lan, C.-W. Changes in the Annual Range of Precipitation under Global Warming. *J. Clim.* **25**, 222–235 (2012).

Acknowledgements

This work was supported by the National Natural Science Foundation of China (grant nos. 42122035, and 42288101). The calculation of this study was supported by the National Key Scientific and Technological Infrastructure project “Earth System Numerical Simulation Facility” (EarthLab).

Author contributions

Methodology: Xiaoqi Zhang, Bian He, Qing Bao. Investigation: Xiaoqi Zhang, Bian He. Visualization: Xiaoqi Zhang. Supervision: Bian He, Guoxiong Wu.

Writing—original draft: Xiaoqi Zhang, Bian He. Writing—review & editing: Xiaoqi Zhang, Bian He, Qing Bao, Yimin Liu, Guoxiong Wu, Anmin Duan, Wenting Hu, Chen Sheng, Jian Rao.

Competing interests

The authors declare no competing interests.

Additional information

Supplementary information The online version contains supplementary material available at

<https://doi.org/10.1038/s41612-024-00717-y>.

Correspondence and requests for materials should be addressed to Bian He or Qing Bao.

Reprints and permissions information is available at

<http://www.nature.com/reprints>

Publisher's note Springer Nature remains neutral with regard to jurisdictional claims in published maps and institutional affiliations.

Open Access This article is licensed under a Creative Commons Attribution 4.0 International License, which permits use, sharing, adaptation, distribution and reproduction in any medium or format, as long as you give appropriate credit to the original author(s) and the source, provide a link to the Creative Commons licence, and indicate if changes were made. The images or other third party material in this article are included in the article's Creative Commons licence, unless indicated otherwise in a credit line to the material. If material is not included in the article's Creative Commons licence and your intended use is not permitted by statutory regulation or exceeds the permitted use, you will need to obtain permission directly from the copyright holder. To view a copy of this licence, visit <http://creativecommons.org/licenses/by/4.0/>.

© The Author(s) 2024